JOURNAL OF SPACECRAFT AND ROCKETS
Vol. 37, No. 1, January–February 2000

Hypersonic Performance of a Lifting Elliptic Cone with and Without Strakes

K. Kontis,* N. Qin,† and J. L. Stollery‡
Cranfield University, Bedfordshire, England MK43 0AL, United Kingdom
and
J. A. Edwards§
Defence Evaluation and Research Agency, Kent, England TN14 7BP, United Kingdom

Side-by-side experimental and computational studies were conducted on a right elliptic cone with and without strakes, and comparisons were made to evaluate the quality of each approach. For the tests the Cranfield University College of Aeronautics hypersonic gun tunnel was employed, at a Mach number of 8.2 and a Reynolds number of 1.76×10^6, based on cone length, using schlieren photography, oil-dot technique, pressure, and forces measurements. The boundary layer was laminar. The computational study employed a three-dimensional, high resolution, iterative, finite volume parabolized Navier–Stokes solver. An estimation model of the aerodynamic forces for the cone with and without strakes was developed based on the standard Newtonian theory.

Nomenclature

a	= major length of an elliptic cross section, m
a	= side length of a square, m
b	= minor length of an elliptic cross section, m
C_A	= axial force coefficient based on the body planform area
C_D	= drag coefficient based on the body planform area, $C_N \sin\alpha + C_A \cos\alpha$
C_{DB}	= base drag coefficient
C_{Df}	= skin-friction drag coefficient
C_L	= lift coefficient based on the body planform area, $C_N \cos\alpha - C_A \sin\alpha$
C_m	= pitching moment coefficient based on the body planform area and the total length
C_N	= normal force coefficient based on the body planform area
C_p	= pressure coefficient
$\boldsymbol{i, j, k}$	= Cartesian unit vectors
L	= length, m
M	= Mach number
p or P	= pressure, N/m^2
R	= residual
Re	= Reynolds number
S	= surface area, m^2
T	= temperature, K
x	= measured distance in x direction, m
x, ρ, φ	= cylindrical polar coordinates
y	= measured distance in y direction, m
z	= measured distance in z direction, m
α	= incidence, deg
γ	= ratio of specific heats
η	= angle between the unit normal and wind vectors, deg
ρ	= density, kg/m^3

Subscripts

c	= cone
max	= maximum
S	= strake
∞	= freestream

Introduction

FUTURE defense weapons may include very high-speed projectiles flying and maneuvering over a wide incidence range. Slender elliptic planform cones are of interest as gun-fired projectiles and investigations[1–3] have shown that they may have important aerodynamic advantages over circular cones. References 4 and 5 performed an experimental and computational study, respectively, on a wing-cone configuration at a freestream Mach number of 5.8. The force results showed that the lift-drag ratio is increased by both the negative and the positive dihedral wings, but the negative dihedral configuration gives a much larger increase in comparison to the simple cone. An investigation[6] on the flow over a wing-cone configuration, similar to Reggiori's[4] model, at a Mach number of 15 found signs of corner vortex flow at the roots of the wings and outflow around the wing leading edges. Levinsky et al.[7] showed theoretically and experimentally that relatively large increases in lift with even the smallest wing sizes, i.e., 10% of the body radius, are possible.

There are a large number of examples of viscous computations[8,9] of body vortex flows, obtained using the full and thin-layer forms of the Reynolds-averaged Navier–Stokes (RANS) equations. These computations are generally time consuming and are not practicable for use in a design environment. The parabolized Navier–Stokes (PNS) equations are a reduced form of the time-marching full three-dimensional RANS equations (the streamwise shear-stress and heat-transfer terms are neglected, and the streamwise flux vector is modified to allow space marching). PNS simulations retain the ability to model viscous effects, such as crossflow separation and allow the use of a space-marching strategy, which reduces both computer execution times and memory requirements. A good demonstration of the capabilities of PNS for the prediction of vortex flows around bodies at high incidence is given by the computations of Degani and Schiff.[10]

The realization that certain flowfields can be computed more accurately than they can be measured experimentally must begin to change the relationship between computational and experimental aerodynamics. This paper addresses this changing relationship and seeks to improve the synergism between computational aerodynamics and wind-tunnel experimentation. [Computational fluid

Presented as Paper 97-2252 at the AIAA 15th Applied Aerodynamics Conference, Atlanta, GA, 23–25 June 1997; received 1 February 1999; revision received 10 September 1999; accepted for publication 10 September 1999.

*Visiting Researcher; currently Engineer Fellow of the European Commission, Gas Dynamics Laboratory, Nagoya University, Nagoya 464-0814, Japan.
†Chair Professor of Computational Aerodynamics, Flow Prediction and Control Group, Cranfield College of Aeronautics. Senior Member AIAA.
‡Professor Emeritus of Aerodynamics, Flow Prediction and Control Group, College of Aeronautics. Fellow AIAA.
§Senior Principal Consultant, WX7 Division, Fort Halstead, Sevenoaks. Senior Member AIAA.

dynamics (CFD) provides more details in the present case.] The physical and numerical approaches can each gain by using the strengths of one approach to offset the weaknesses of the other and vice versa.

Experimental Setup and Model Geometry

The experiments were conducted in the College of Aeronautics gun tunnel, with air as freestream gas. An axisymmetric contoured nozzle provided a flow at $M_\infty = 8.2$, $Re_\infty = 9.3 \times 10^6$/m, $T_\infty = 89.3$ K, $P_\infty = 950.3$ N/m^2, and $\rho_\infty = 0.0371$ kg/m^3. The numerical simulations and experiments assumed an average wall temperature of 296 K. A description of the setup and calibration of the facility are given by Refs. 11–13. The flow is uniform inside the test section except on the centerline,[13] where the Mach number varies by ±4.5%. Pressure measurements were carried out using absolute pressure transducers with estimated error of ±5%. Discrete oil dots were applied on the matt black painted surface of the models. Direct measurement of the effect of strakes on aerodynamic performance has been made using a three-component balance having an accuracy of normal force and pitching moment ±1.5% and of axial force ±2% (Ref. 13). A repeatability of 97%, of the force and moment coefficients, was achieved in the present investigation over six runs.

The models were a pair of right elliptic cones, $a/b = 1.6$, with and without strakes, shown in Fig. 1, mounted on a 0.004-m radius stainless-steel sting of 0.15 m length. The strakes were 0.003 m square at base requiring the extension to the nose of the body by tapering them to zero height at the nose but keeping the width constant up to 0.1725 m from the base and then conical to zero at nose. This strake geometry allows a great simplification in body geometry description and outflow boundary conditions in the numerical simulation eliminating unnecessary numerical difficulties. It also simplifies manufacture. The instrumentation consisted of 10 pressure taps located on the models as shown in Fig. 1.

CFD Code

The numerical study employs a three-dimensional, high-resolution, iterative, finite volume PNS solver (Cranfield PNS3D).[13,14] The region of interest is discretized into small but finite hexahedral cells denoted by $\boldsymbol{i}, \boldsymbol{j}$, and $\boldsymbol{k}$. The conservation integral is applied to cell $\boldsymbol{i}, \boldsymbol{j}, \boldsymbol{k}$, and the assumption is made that the flux tensor remains constant across each face of the cell. The numerical integration procedure produces cell-averaged flow properties, which are assigned to the centers of each of the hexahedral cells. The flux vectors are evaluated at the cell interfaces from the two distinct sets of state quantities on either side of the cell interface. Second- or third-order spatial accuracy is achieved via the MUSCL interpolation with a flux limiter to avoid oscillations at discontinuities such as shock waves. The Baldwin–Lomax[15] algebraic turbulence model with the modification proposed by Degani and Schiff[10] is employed to provide a turbulent contribution to the viscosity. The inviscid fluxes are computed using the approximate Riemann solver of Osher and Chakravathy.[16] This scheme has been demonstrated[17] to be effective in capturing both shock waves and shear layers in compressible viscous flows.

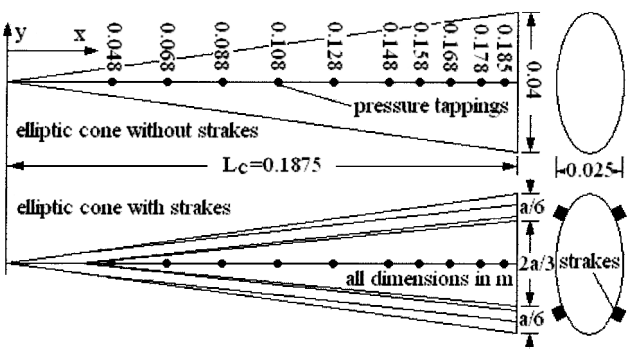

Fig. 1 General geometry of the models.

After transforming the governing equations from a system of partial differential equations to a system of ordinary differential equations in the streamwise marching coordinate, a fully implicit integration method is adopted.[13] The choice of an implicit marching strategy removes the need to consider stability restrictions when determining the size of the streamwise marching step. The viscous fluxes at the cell interfaces are evaluated using Gauss's theorem for the gradient at the cell interfaces. The streamwise fluxes are purely inviscid. The pressure terms in the equations are modified using the approach of Vigneron et al.,[17] to prevent upstream influence within the subsonic boundary layer and eliminate departure solutions. The streamwise flux is calculated in an upwind fashion using the states at the cell centers upstream. A pseudotime term is introduced at each station to solve the resulting nonlinear system. The pseudotime dependent term is discretized using a first-order-accurate Euler explicit method. At each streamwise station the discretized equations are marched forward in pseudotime, using a time step determined from the local Courant–Friedrichs–Lewy condition, until a converged steady-state solution is obtained.

On the body surface the no-slip and isothermal wall conditions are applied. The values along the singular axis are obtained by averaging the values on the upper and lower symmetry planes, whereas at the outer boundary the freestream condition is enforced. At the downstream boundary the values are extrapolated from inside the solution domain. The initial data at the first streamwise station are generated through iteration under the assumption that the flow is locally conical. Basically the method solves a series of two-dimensional problems marching down.

Birch et al.[14] assessed the effect of the simplifying assumptions, which are incorporated within the PNS solver, to enable the use of a space-marching strategy by a computation using a three-dimensional time-marching RANS solver for comparison with the PNS solution. The agreement between the two codes was very good, justifying the use of the PNS approach for missile aerodynamics computational studies. The PNS solver has also been validated[18] to a missile configuration tested experimentally at a Mach number of 8.2.

Estimation Model of Aerodynamic Forces and Moments

Elliptic Cone Without Strakes

The force and moment coefficients, for the body without strakes, were estimated using the closed-form expressions from Wells and Armstrong.[19]

Elliptic Cone with Strakes

The strakes were assumed to be square cross-section cones of half-angle 0.7 deg and total length of 0.188 m. Any vortices caused by boundary-layer separation and regions of trapped flow, such as at the strake-body junction, were neglected. The contribution of the strakes to the aerodynamic forces and moments was neglected if they were located inside the shadow region of the elliptic cone. The contribution of areas of the main body to the aerodynamic forces and moments, occupied by strakes or located inside the strakes shadow region, was subtracted from the total values. With the basic cone at 0-deg incidence, each strake was assumed to be at an incidence of 4.27 deg and a sideslip angle of 4.19 deg with respect to the velocity vector. The derivation started from the Newtonian relation $C_p = 2\cos^2\eta$. To determine the unit normal vector, the equation of the body surface must be derived in a suitable coordinate system, that is, $f = g(x, y, z)$. The unit normal vector was expressed as the gradient of the surface divided by its magnitude.[13] The unit wind vector $\boldsymbol{V}\,(= -\cos\alpha\cos\beta\boldsymbol{i} - \sin\beta\boldsymbol{j} - \sin\alpha\cos\beta\boldsymbol{k})$ was expressed in terms of the body axis.[13] The value of $\cos\eta$ was then determined by taking the dot product of the unit normal and wind vectors. In this analysis the coordinate axis system was chosen with positive directions x, y, and z as forward, to the right, and downward, respectively, when viewed from the rear of the body. For purposes of integration, cylindrical coordinates were used (see Fig. 2): $x = x$, $y = -\rho\sin\varphi$, $z = -\rho\cos\varphi$. The force and moment coefficients were obtained by

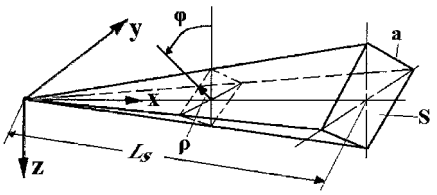

Fig. 2 Strake coordinate system.

performing numerical integration using the pressure coefficient as determined by Newtonian theory:

$$C_N = -\frac{L_S}{S}\int_0^{-L_S}\int_{\varphi_i}^{\varphi_f}\frac{C_p a x\,\sin(135-2\varphi)}{2L_S\sin^2(135-\varphi)}\,\mathrm{d}\varphi\,\mathrm{d}x \tag{1}$$

$$C_A = -\frac{L_S}{S}\int_0^{\rho_b}\int_{\varphi_i}^{\varphi_f}\frac{C_p\,\rho(\cos^2\varphi-\sin^2\varphi)}{2}\,\mathrm{d}\varphi\,\mathrm{d}\rho \tag{2}$$

$$C_m = -\frac{1}{L_S S}\left(\int_0^{\rho_b}\int_{\varphi_i}^{\varphi_f}\frac{C_p\,\rho^2\cos\varphi(\cos^2\varphi-\sin^2\varphi)}{2}\,\mathrm{d}\varphi\,\mathrm{d}\rho + \int_0^{L_S}\int_{\varphi_i}^{\varphi_f}-\frac{C_p(L_S+x)ax\,\sin(135-2\varphi)}{2L_S\sin^2(135-\varphi)}\,\mathrm{d}\varphi\,\mathrm{d}x\right) \tag{3}$$

The integration was restricted to the regions that see the flow, that is, regions where $\cos\eta \geq 0$. Therefore, the limits of integration φ_i and φ_f were determined as the points on the base of the strake where shadow begins and are given by setting $C_p = 0$. If the surface of the strake is in contact with the elliptic cone at these points, then the body limit forms the limits of integration. The total force and moment coefficients, for each incidence, e.g., lift coefficient, were predicted according to

$$C_{L\,\text{total}} = \sum_{\text{strakes}} C_{L_S} + C_{L_c} \tag{4}$$

This method for deriving the individual forces and moments fundamentally assumes that the forces and moments generated in the presence of strakes are equal to the sum of the individual components, i.e., the algebraic sum of the forces and moments generated by the cone and the strakes.

Results and Discussion

Grid Generation

The flowfield of the elliptic cone with and without strakes was simulated, assuming a perfect gas and a laminar boundary layer over the full length of the body for incidences 10, 15, and 20 deg. The Navier–Stokes solution converged after about 6000 iterations. The convergence to the steady-state solution was checked by monitoring the flowfield parameters residuals. The important parameters are the pressure coefficient and the rate of heat transfer to the body along the top, leeward, and windward meridians. From the convergence histories, the inviscid parameters such as the pressure coefficient were found to have achieved steady state before the viscous parameters such as the rate of heat transfer to the body. The solution was considered to be converged when $\|R(\boldsymbol{Q})\| \leq \varepsilon$, where $\varepsilon = 10^{-4}$ or the maximum number of iterations is satisfied. ($\boldsymbol{Q}$ is the vector of conserved variables.)

The computational grids were generated using a three-dimensional transfinite interpolation technique.[20] For complicated geometries like the elliptic cone with strakes, a multiblock grid is normally used, but in the present study all of the grids were single-block H-O type grids (H in the $\boldsymbol{i}$ direction and O in the $\boldsymbol{k}$ direction), see Figs. 3a and 3b. The grid was generated in the following order:

1) Generation of the one-dimensional line grids at all junctions of the domain surfaces with the appropriate stretching according to the curve length[13] occurred.

2) Generation of the two-dimensional surface grids for all of the domain boundary surfaces using the one-dimensional line grids as the interpolation boundaries and applying any geometric constraints where necessary occurred.

3) Generation of the three-dimensional field grid by interpolation of the surface grids and ensuring the orthogonality of the grid at the wall by specifying the derivative information at the wall occurred. The cluster of the grid at the wall was controlled by either the magnitude of the derivative or the stretch factor in the interpolation.[13]

4) A three-dimensional elliptic smoother was used to smooth the grid in regions where this is critical, i.e., around the sharp corners of the strake.[13] The grid points generated are the vertices of the hexahedral cells in the finite volume formulation. A secondary grid is created by the central points of the cells for the presentation of the results from the finite volume solution.

Because the forces and moment coefficients are the main parameters that are compared with experimental data, they are used as the representative factors for the sensitivity of the numerical solution to the computational grid of the cone with strakes (Fig. 4). Smoothing and stabilizing parameters were kept to a minimum during the

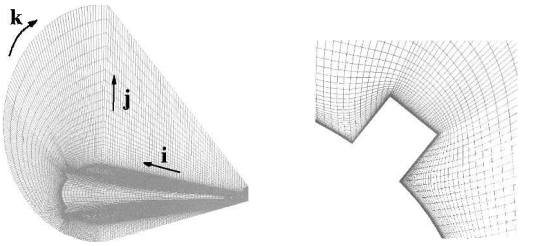

a) Overall computational grid **b) Grid around strake**

Fig. 3 Computational grid for the elliptic cone with strakes.

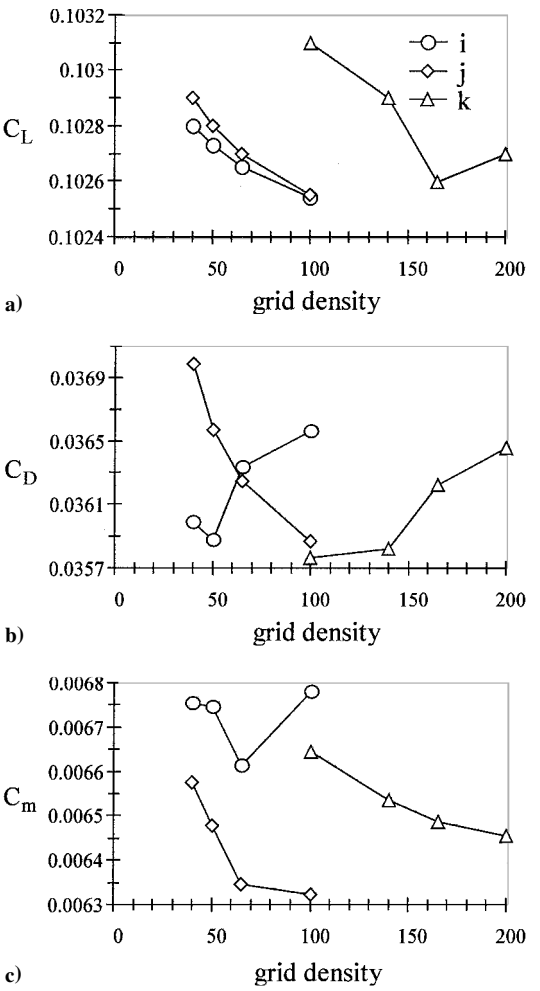

Fig. 4 Sensitivity of aerodynamic forces and moment to grid density.

grid-sensitivity studies. The grid is refined in each direction of the three dimensions while holding the other two dimensions fixed. The study showed considerable sensitivity of the calculated forces and moment coefficients in the streamwise direction. This is attributed to the integration routines, which have been used to evaluate the forces and moments. This is a conjecture and needs further investigation. The results of this study suggested that 165 grid points placed in the circumferential direction (k) and 65 grid points in each of the other directions (i and j) might be sufficient to resolve the flow features of interest for the elliptic cone with strakes (see Figs. 3a and 3b). This grid is highly clustered in the radial direction toward the wall and yields a typical value of $y+ < 1$ for the first cell off the body surface for better resolution of the viscous layer. A $64 \times 65 \times 65$ half circumference grid was used for discretization of the flowfield of the elliptic cone alone.

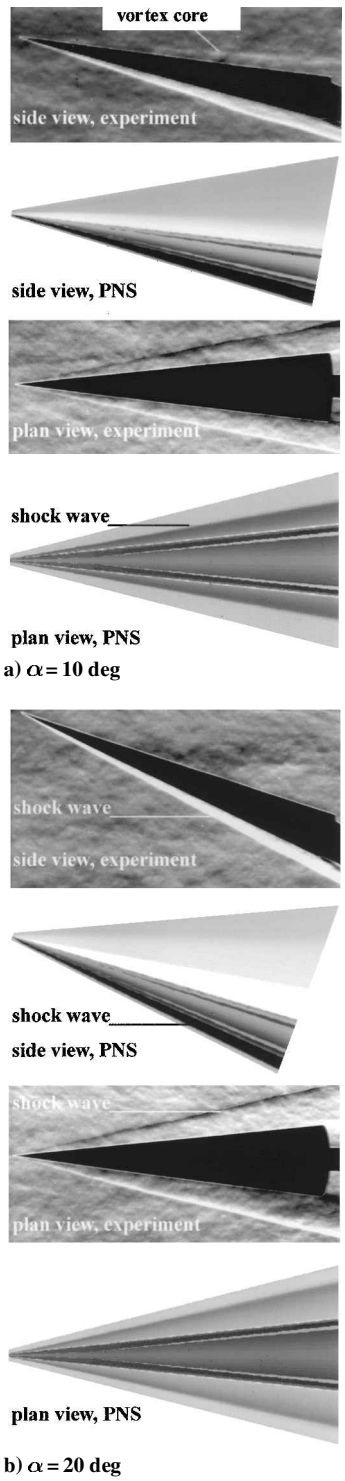

Fig. 5 Comparison of the schlieren pictures for $\alpha = 10$ and 20 deg cases with the numerical results.

Flow Visualization Results

At low incidences the axial flow velocity is dominant, and the flow is attached.[13] With increasing incidence the boundary layer over the leeward side thickens, and the crossflow strength on the windward side increases because of the increasing crossflow velocity component with incidence.[13] There is the establishment of a disturbed flow region over the leeward side close to the rear of the cone, which moves forward toward the tip of the body. The separated crossflow results in the establishment of a pair of counter-rotating vortices over the leeside of the body.[12,13] At $\alpha = 10$ deg, Fig. 5a (side view, experiment), the separation region extends over the whole length. In the same figure the white line nearer the surface on the leeward side indicates the vortex core. At $\alpha = 15$ deg, the PNS study, e.g., in Figs. 6a and 7c, also shows the existence of a vortical flow over the leeward side. At 20-deg incidence, Fig. 5b (side view, experiment), the vortex appears to have burst. Because the sting is only a fraction of the base area (about 6% of the cone base area; see the Experimental Setup and Model Geometry section), the vortex bursting in this case is a genuine flow phenomena. The numerical pictures in Fig. 5 exhibit the density of the flow. The computational plane, which is shown in the numerical schlieren pictures, corresponds to the plane, which contains the minor axis. The experimental schlieren pictures in the same figure are focused on the same plane but do respond to some extent to all density gradients in the beam path. The computational study predicts satisfactorily the experimental shock shapes for all incidences under consideration and the fact that the windward shock is getting closer to the body surface as incidence is increasing. The experimental and numerical schlieren plan views do not reveal any detailed flow characteristics. However, they show

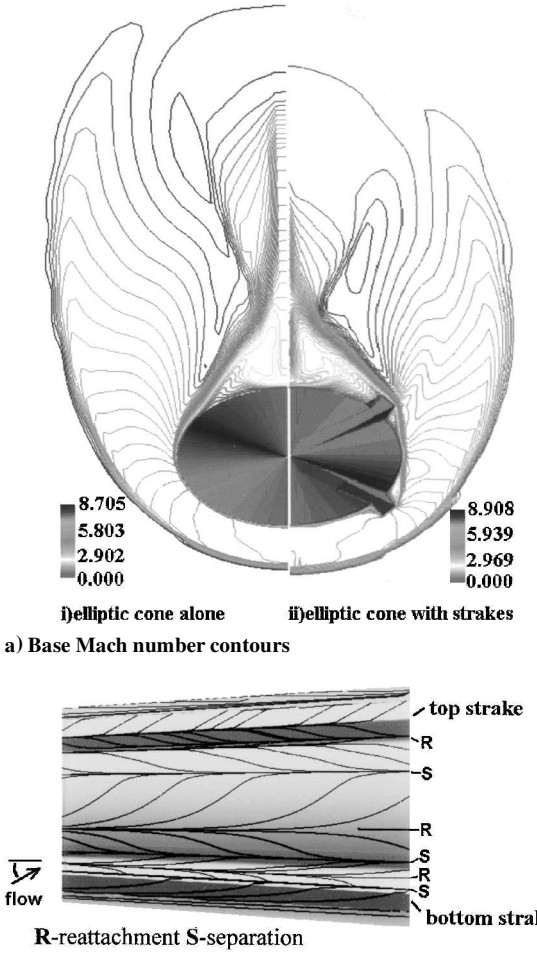

Fig. 6 Some computational flowfield results for $\alpha = 15$ deg case.

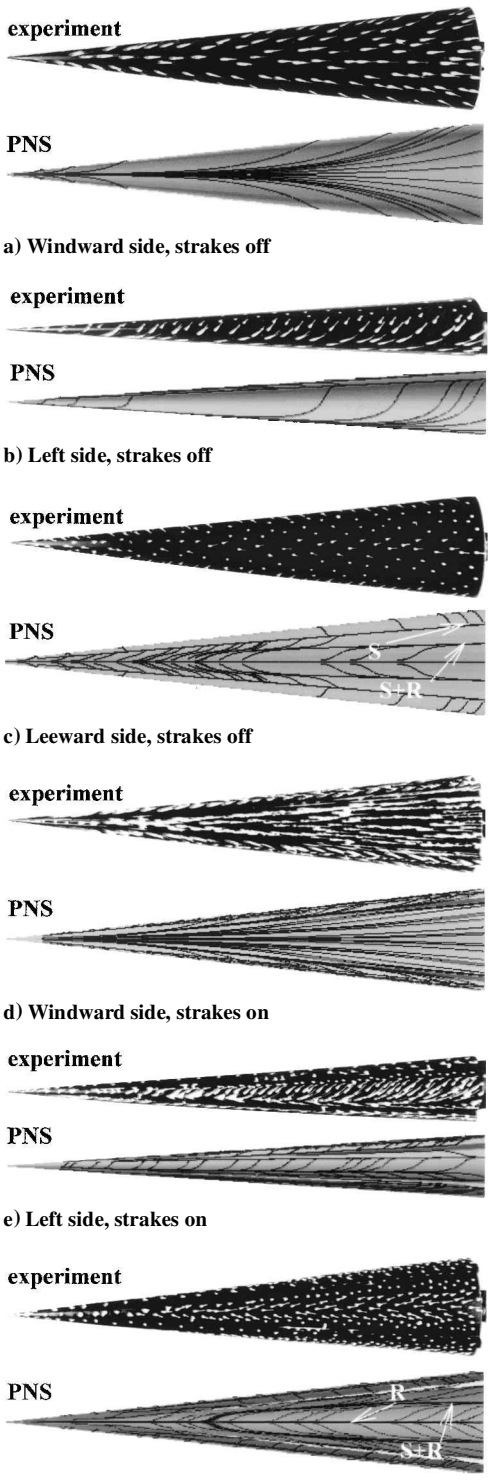

Fig. 7 Comparison of the oil-dot flow visualization and numerical streamline results for the cone with and without strakes for $\alpha = 15$ deg case: S = separation; R = reattachment.

that the distance between the cone surface and the shocks envelope is increasing with incidence.

The typical flowfield characteristics for the cone with and without strakes as predicted by the PNS solver are shown in Fig. 6a, $\alpha = 15$ deg case. The Mach-number contours show the relative position of the circumferential boundary layer, which is thin over the windward side and thickens as the flow expands. For the cone without strakes, Figs. 7a–7c show that the flow separates after the end of the major axis and reattaches at the top leeward meridian and then diverges. The PNS study, Fig. 7c, shows a secondary separation to take place over the leeward side. The flow separation lines from which the vortices are fed also trace an essentially linear path along the model surface. In the region of the separation line, an interaction is established between the flow that has separated and the approaching inviscid flow. If the resultant Mach number associated with the elevational and circumferential velocity components exceeds one, there will be an imbedded shock-wave system on the leeward side of the cone. The examination of the predicted flowfields for the cone with and without strakes, Fig. 6a, suggests the existence of an imbedded shock wave on the leeward side, above the vortex. The PNS calculation of the windward side flowfield, Fig. 7d, captures successfully the inhibiting effect of strakes to the crossflow. Because strakes inhibit the crossflow, the body shock becomes stronger, and the envelope moves further away from the body surface on the windward side. This is well demonstrated by the PNS results shown in Fig. 6a, where the numerical comparison for the cone with and without strakes shows a difference in the shock angles, strakes on and off, of approximately 0.5 deg. However, the experimental comparison[13] shows no gross external flow differences caused by the addition of strakes. The numerical predictions of the position of the main separation and reattachment lines agree quite well with the oil-dot study. The computation reveals a very complicated flow, which in some regions, especially for the cone with strakes, the separation and reattachment lines occur very close to each other, Fig. 6b. The oil-dot technique is not able to capture all the flow phenomena in such a detail as the numerical study. With increasing incidence the strakes greatly inhibit the crossflow on the windward side.[13]

Pressure Measurements

Figures 8a and 8b display the effect of strakes on the pressure distributions along the top windward and leeward meridians for $\alpha = 10$ and 20-deg cases. On the windward side, Fig. 8a, the percentage of increase in pressure caused by the strakes addition increases with incidence. The effectiveness of the strakes increases with incidence because of the increasing crossflow component on the windward side they can block.[13] Conversely on the leeward side, Fig. 8b, the expansion of the flow over the leeward surfaces of the other two strakes having positive dihedral reduces the pressure on the leeward side of the body in comparison with the pressure there for the body-alone configuration. The percentage of reduction in pressure caused by the strakes addition decreases with incidence. This decreasing percentage of reduction in pressure with incidence is because the top

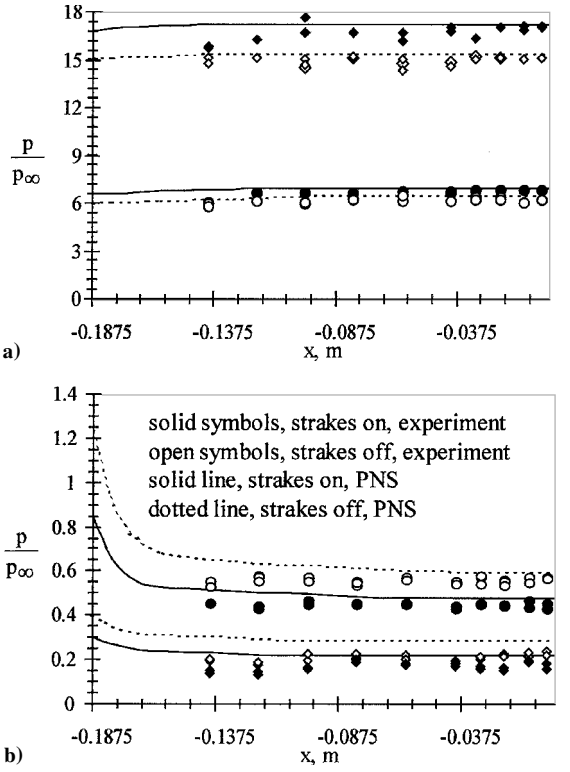

Fig. 8 Comparison of numerical and experimental pressure distributions.

strakes act on a separated region, and as the separation point moves round with incidence, their effect is getting smaller. The numerical results show good agreement with the experimental pressure distributions along the windward meridian both with and without strakes. The PNS solver predicts a slight gradual decrease of the pressure distribution toward the tip of the cone. The rate of this decrease is getting higher with incidence. Palko and Ray[2] also found this effect in their experiments. Because of the lack of extra pressure tappings near the nose, it is not possible to confirm this in the present investigation. Along the leeward meridian the numerical results seem to overpredict the experimental pressure distributions for the cone with and without strakes.

As was discussed in the Flow Visualization Results section, the CFD study predicted that adding strakes to an elliptic cone, e.g., $\alpha = 15$ deg, causes an increase in the windward shock angle of about 0.5 deg (4%). The equivalent sharp cone half angle, for the elliptic cone without strakes at $\alpha = 15$ deg, is 18.8 deg. From Ames tables[21] this cone semivertex angle corresponds to a surface pressure ratio of $p/p_\infty = 11.4$ and a shock angle of about 21.9 deg. Hence the shock angle of the equivalent sharp cone, for the elliptic cone with strakes at $\alpha = 15$ deg, is 22.4 deg. From the tables[21] this shock angle corresponds to an equivalent sharp cone semivertex angle of 19.5 deg and a surface pressure ratio of $p/p_\infty = 12.2$. This simple method predicts an increase of pressure of about 7% caused by strakes for the elliptic cone at $\alpha = 15$ deg. The experimental study[13] found a 10% increase caused by strakes at $\alpha = 15$ deg.

Forces and Moment Measurements

The effect of strakes is to increase the C_L-α curve slope, Fig. 9a. This increase is caused by increased pressure over the lower side of the cone (see the Pressure Measurements section). Generally speaking, the favorable interference created by the strakes causes an increase in the lift coefficient at all incidences tested. Basically the strakes act as very small wings. The lift curve is nonlinear, the separation of the leeside flow further increases the slope caused by increased suction over the leeward side of the cone, Figs. 8b and 9a. Figure 9b shows that adding strakes increases the C_D values at all incidences tested. This increase is small particularly at the lower incidences because the addition of strakes does not change the nose shape, and hence the nose shock[13] and any increase in the drag coefficient caused by comparatively small strakes is therefore expected to be small. Adding strakes increases the curve slope of the pitching moment coefficients about the balance moment center, Fig. 9c (the pitching moments were measured at the moment reference point located at $x/L_c = -0.28$ along the body axis measured from the base). As incidence increases, there is an increase in the pitching moment coefficient because the increase in the lift coefficient for the cone with strakes over that without the strakes continues to increase with α.

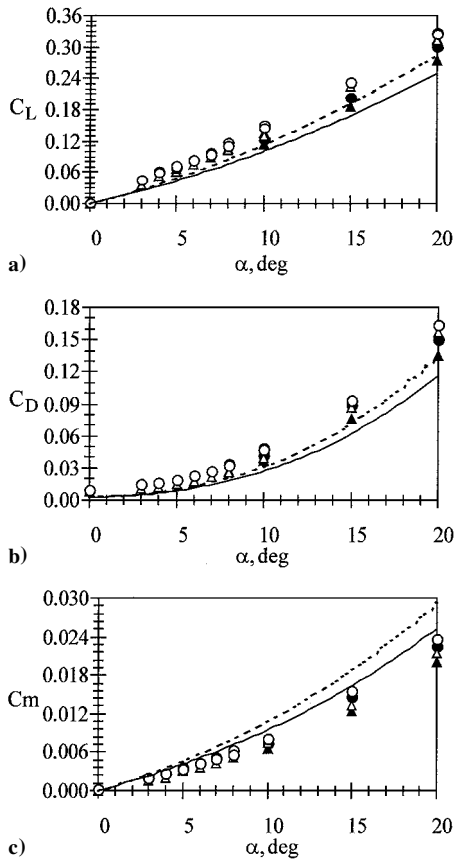

Fig. 9 Effect of strakes on the aerodynamic characteristics: ▲, PNS, strakes off; ●, PNS, strakes on; △, experiment, strakes off; ○, experiment, strakes on; ——, theory, strakes off; and – – –, theory, strakes on.

Both theory and computation successfully predicted the experimental trends, Fig. 9; however, they underpredict the magnitude of C_L and C_D and forecast a higher increase in the lift and drag coefficients caused by the strakes. The theoretical model overpredicts the magnitude of C_m. The computation exhibits better agreement with the experimental results than theory, especially at lower incidences. The increasing importance of vortical flow (see Flow Visualization Results section) and the resulting nonlinearity, as incidence is increasing further, causes a deterioration in the comparison of both calculation and theory with experiment. The larger discrepancies between the PNS solution and the experimental data at higher incidences may be caused by 1) a decreased accuracy of the PNS approximation with an increased incidence, 2) an increased measurement error at higher incidences, and 3) the possible occurrence of vortex burst at higher incidences, which is not modeled in the PNS solution. The differences can probably be reduced, for example, inputting more detailed knowledge of the boundary-layer state over the cone. The numerical study does not take into account the effects of the base drag into the calculations. The theoretical models do not include the effects of the base drag and skin-friction drag. An indication of the value of the base drag coefficient is given by $C_{DB\,max} = 2/\gamma M_\infty^2 = 1.43/M_\infty^2$. For example, at 20-deg incidence the addition of the base drag component causes the predicted lift coefficients by computation and theory to decrease by 0.004 (this is the maximum contribution to the lift coefficients for the incidences under consideration). For the elliptic cone without strakes,[13] $C_{Df} = 0.0006$. For the elliptic cone with strakes,[13] $C_{Df} = 0.0007$.

Conclusions

The numerical study predicted the complex flowfield surrounding the elliptic cone and gave a better understanding of the complicated nature of the flow and good indications of the shock shape and vortex core positions. It successfully predicted the inhibiting effect of strakes on crossflow, the reduction of pressure on the leeward side, and the increase of pressure on the windward side caused by strakes and that addition of strakes produces a significant increase in the lift and drag coefficients. However, the actual predicted values were in poor agreement with experiment.

In the experimental design stage CFD can be used to identify important areas and important flow conditions before the model is cut, which can save unnecessary waste in the experimental tests. After data collection from the experiments, detailed numerical simulation can be conducted for the experimental conditions. In the present study the simulation was able to provide flowfield information to enhance the understanding of the experimental results.

An estimation model of the aerodynamic forces and moments for the right elliptic cone with strakes was developed based on the standard Newtonian theory. The model successfully predicted the experimental trends in the aerodynamic coefficients caused by strakes addition.

Acknowledgments

The work was supported under contract by the U.K. Defence Research Establishment and Research Agency. The pressure measurements were carried out using Kulite XCS-190 absolute pressure transducers. A Silicon Graphics workstation Indigo-2 was used for the computational study.

References

[1]Van Dyke, M. D., "The Elliptic Cone as a Model for Non-Linear Supersonic Flow Theory," *Journal of Fluid Mechanics*, Vol. 1, Pt. 1, May 1956, pp. 1–15.

[2]Palko, R. L., and Ray, A. D., "Pressure Distribution and Flow Visualization Tests of a 1.5 Elliptic Cone at Mach 10," Arnold Engineering Development Center, AEDC/TDR-63/163, Aug. 1963.

[3]Graves, E. B., "Aerodynamic Characteristics of a Monoplanar Missile Concept with Bodies of Circular and Elliptical Cross Sections," NASA TM-74079, Dec. 1977.

[4]Reggiori, A., "Lift and Drag of Wing-Cone Configuration in Hypersonic Flow," *AIAA Journal*, Vol. 9, No. 4, 1971, pp. 744, 745.

[5]Chaudhry, S. R., Qin, N., and Richards, B. E., "Hypersonic Viscous Flows Around Waverider Configurations," *Proceedings of the First International Hypersonic Waverider Symposium/Maryland*, edited by J. D. Anderson, I. M. Blankson, S. Corda, and M. J. Lewis, Univ. of Maryland, College Park, MD, 1990, pp. 33–41.

[6]Houwink, R., and Richards, B. E., "Experimental Study of a High Lift Reentry Vehicle Configuration," *AIAA Journal*, Vol. 11, No. 5, 1973, pp. 749–751.

[7]Levinsky, E. S., and Wei, M. H. Y., "Non-Linear Lift and Pressure Distribution of Slender Conical Bodies with Strakes at Low Speeds," NASA CR-1202, Oct. 1968.

[8]Baysal, O., Fouladi, K., and Miller, D. S., "Computations of Supersonic Flows over a Body at High Angles of Attack," *AIAA Journal*, Vol. 27, No. 4, 1989, pp. 427–437.

[9]Graham, J. E., and Hankey, W. L., "Computation of the Asymmetric Vortex Pattern for Bodies of Revolution," AIAA Paper 82-0023, Jan. 1982.

[10]Degani, D., and Schiff, L. B., "Computation of Turbulent Supersonic Flows Around Pointed Bodies Having Crossflow Separation," *Journal of Computational Physics*, Vol. 66, No. 1, 1986, pp. 173–196.

[11]Stollery, J. L., Maull, D. J., and Belcher, D. A., "The Imperial College Hypersonic Gun Tunnel," *Journal of the Royal Aeronautical Society*, Vol. 64, Dec. 1960, pp. 24–30.

[12]Kontis, K., and Stollery, J. L., "Control Effectiveness of a Jet–Slender Body Combination at Hypersonic Speeds," *Journal of Spacecraft and Rockets*, Vol. 34, No. 6, 1997, pp. 762–768.

[13]Kontis, K., "Projectile Aerodynamics: Measurement and Computation," Ph.D. Dissertation, Flow Control and Prediction Group, Cranfield College of Aeronautics, Cranfield Univ., Bedfordshire, U.K., Oct. 1997.

[14]Birch, T. J., Qin, N., and Jin, X., "Computation of Supersonic Viscous Flows Around a Slender Body at Incidence," AIAA Paper 94-1938, June 1994.

[15]Baldwin, B. S., and Lomax, H., "Thin-Layer Approximation and Algebraic Turbulence Model for Separated Turbulent Flows," AIAA Paper 78-257, Jan. 1978.

[16]Osher, S., and Chakravathy, S. R., "Upwind Schemes and Boundary Conditions with Applications to Euler Equations in General Co-ordinates," *Journal of Computational Physics*, Vol. 50, No. 3, 1983, pp. 447–481.

[17]Vigneron, Y. C., Rakich, J. V., and Tannehill, J. C., "Calculation of Supersonic Viscous Flow over Delta Wings with Sharp Leading Edges," AIAA Paper 78-1137, Jan. 1978.

[18]Edwards, J. A., and Roper, J. J., "A Computational Assessment of Static and Dynamic Coefficients for the H3 Hypervelocity Projectile, AIAA Paper 97-0640, Jan. 1997.

[19]Wells, W., and Armstrong, W., "Tables of Aerodynamic Coefficients Obtained from Developed Newtonian Expressions for Complete and Partial Conic and Spherical Bodies at Combined Angles of Attack and Sideslip with Some Comparisons with Hypersonic Experimental Data," NASA TR-R-127, Jan. 1962.

[20]Eiseman, P. R., "Grid Generation for Fluid Mechanics Computation," *Annual Review of Fluid Mechanics*, Vol. 17, Feb. 1985, pp. 487–522.

[21]"Equations, Tables and Charts for Compressible Flows," NACA Rept. 1135, Jan. 1953.

R. M. Cummings
Associate Editor